February 24, 2003
CERN/SPSC 2003-010
SPSC-M-695

ASACUSA STATUS REPORT

ASACUSA progress during 2002
and plans for 2003

ASACUSA collaboration

Contents

Part I
ASACUSA Progress during 2002

1 Spectroscopy of Antiprotonic Helium

1.1 High-precision laser spectroscopy of isolated $\overline{p}\mathrm{He}^+$, and a new limit on the antiproton charge and mass

In 2002, we measured twelve atomic transition frequencies in $\overline{p}^4\mathrm{He}^+$ and $\overline{p}^3\mathrm{He}^+$ atoms to a fractional precision of 8×10^{-8} in the best case, using laser spectroscopy. By comparing these results with QED calculations and the antiproton cyclotron frequency measured by the TRAP collaboration, we set a new limit of $\sim 1 \times 10^{-8}$ (preliminary value) on the possible differences between the antiproton and proton charges and masses. These higher-precision experiments were made possible by new experimental techniques involving a radiofrequency quadrupole decelerator (RFQD) and a magnetic achromatic spectrometer (Fig. 1).

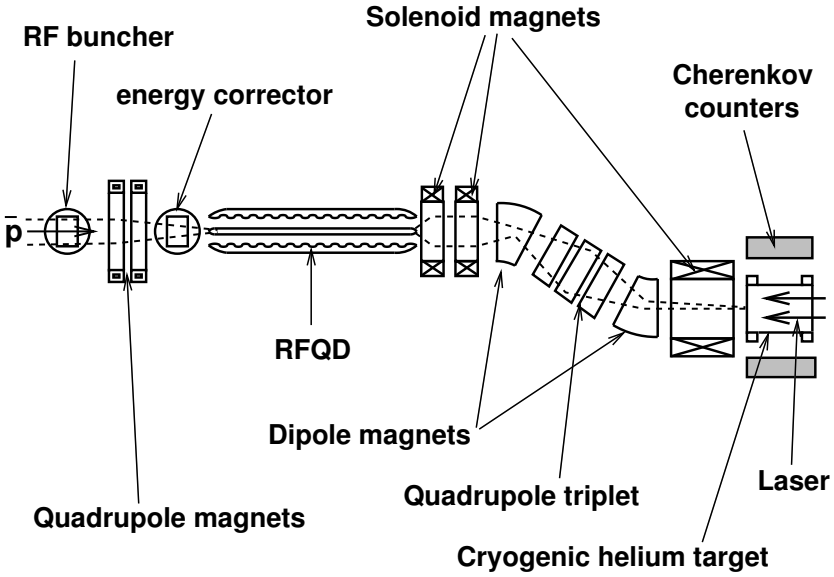

Figure 1: Experimental layout. Drawing not to scale.

Now the precision of past experiments [1] made by the ASACUSA collaboration were limited by the high density of the cryogenic helium targets ($\rho \sim 10^{21}$–10^{22} cm^{-3}, corresponding to 20–200 Bars at room temperature) used to stop the high-energy ($T = 5.3$ MeV) antiproton beam of AD. The $\overline{p}\mathrm{He}^+$ atoms consequently made many collisions with the surrounding helium atoms, which caused large shifts [2] in the transition frequencies ($|\Delta\nu| = 0.5$–5.0 GHz) corresponding to fractional changes between 10^{-6} and 10^{-5}. The frequencies $\nu_{\rho=0}$ for an isolated atom in vacuum had to be inferred by repeating the measurements at higher densities and assuming a linear extrapolation to $\rho = 0$. Some of these experimental values diverged significantly from theory; for example, the transition with the largest density shift

$((n,\ell) = (39,35) \rightarrow (38,34)$ at a wavelength of $\lambda = 597.3$ nm) disagreed with theoretical values by $(5-7) \times 10^{-7}$ [1].

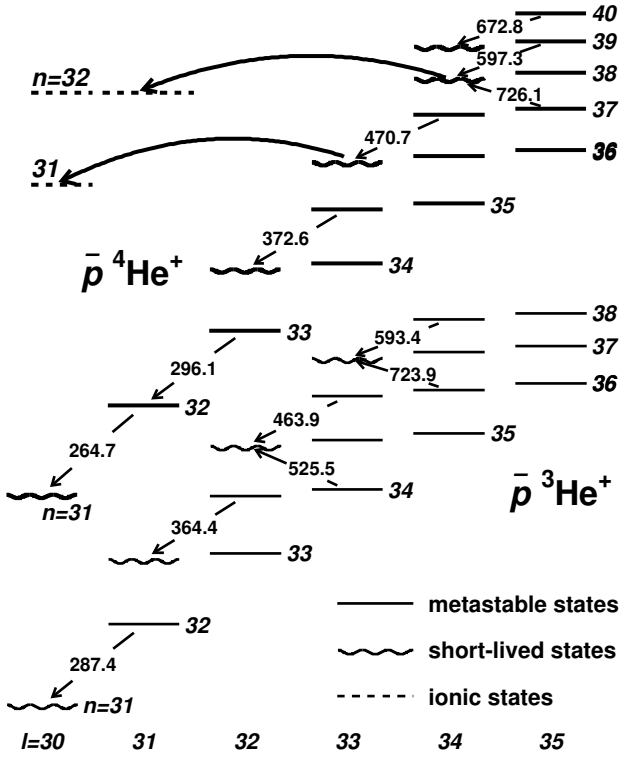

Figure 2: Energy level diagrams of $\overline{p}^4\mathrm{He}^+$ and $\overline{p}^3\mathrm{He}^+$ atoms. Wavelengths of studied transitions are indicated in nanometers.

In the experiment made in 2002, the RFQD decelerated the 5.3-MeV antiproton beam of AD to energies $T < 100$ keV, so that the $\overline{p}\mathrm{He}^+$ atoms could be produced in targets with densities $\rho \sim 10^{16}$ cm^{-3}, which is 10^4–10^6 times lower than the previously used densities [1]. The collisional shifts ($\Gamma < 1-10$ MHz) thus became negligible compared to the natural widths of the transitions, and the in-vacuo frequencies were directly observed without extrapolation. An achromatic spectrometer was used to divert only the decelerated antiprotons, and focused them into a 5-mm-diam spot at the entrance of the experimental target; we thus avoided the large background that the undecelerated antiprotons would have otherwise produced. The spectrometer consisted of two dipole magnets which bent the beam twice in the horizontal plane at an angle $\theta = 20°$, three 1-T solenoids which focused the beam, and three quadrupole magnets which transferred the focal point of the beam at the exit of the RFQD to the position of the experimental target. The spatial profile of each antiproton pulse was measured non-destructively by four micro-wire secondary electron emission detectors positioned along the beam line.

The target was a 15-cm-diam, 30-cm-long cylindrical chamber filled with ^{4}He or ^{3}He gas, at pressures of $P = 0.05$–2 mb and temperatures of $T = 12$–30 K. The antiprotons entered the target through a 0.8-μm-thick polyethylene foil. The antiprotons diffused and filled the entire volume of the chamber, and formed $\overline{p}\mathrm{He}^+$ atoms. The atoms were irradiated by a laser beam with a diameter $d = 3$–5 cm entering the chamber through a fused silica window.

Charged pions emerging from the annihilations produced Cherenkov light in two 2-cm-thick Lucite plates. By detecting this light envelope using a photomultiplier and recording its waveform with an oscilloscope, the delayed annihilation time spectra (the distribution of the number of antiproton annihilations, as a function of time elapsed since atomic formation) was observed. Annihilation spikes could be induced on the spectrum, at any time $t = 0.3$–15 μs after formation (Fig. 3 (a)).

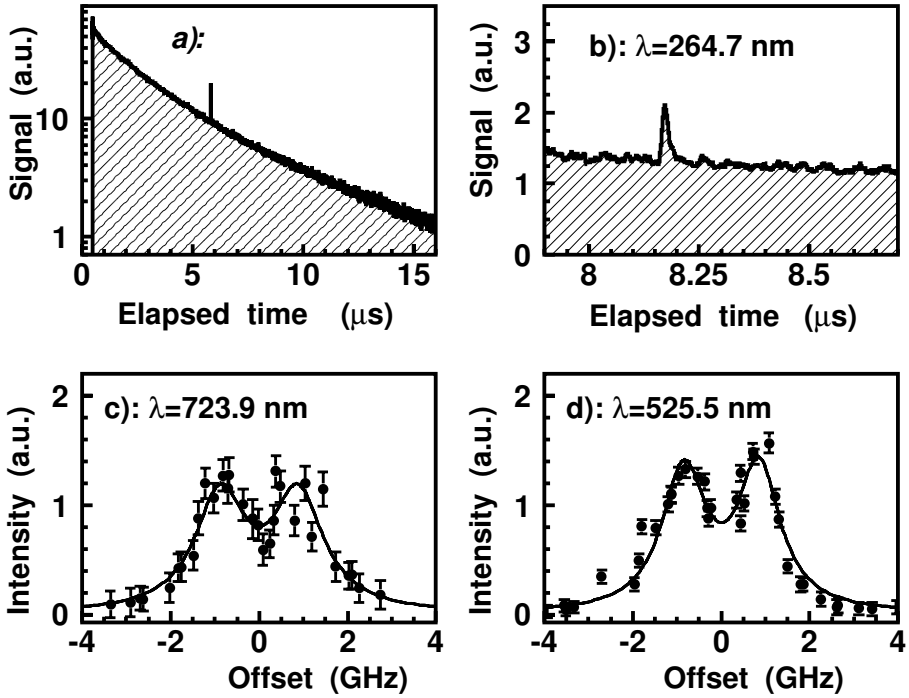

Figure 3: Delayed annihilation time spectrum measured at ultra-low densities (a). Laser-induced annihilation spike of the $\overline{p}^4\mathrm{He}^+$ transition $(32,31)\rightarrow(31,30)$ (b). Frequency profiles of the $\overline{p}^3\mathrm{He}^+$ transitions $(36,34)\rightarrow(37,33)$ in $\overline{p}^3\mathrm{He}^+$ (c) and $(34,33)\rightarrow(35,32)$ in (d), see text.

In Fig. 3 (c), the resonance profile of the $\overline{p}^3\mathrm{He}^+$ transition $(36,34)\rightarrow(37,33)$ at 723.9 nm is shown. The two-peak structure is the hyperfine splitting [3, 4] arising from the interaction between the orbital angular momentum of the antiproton and the electronic spin. The measured spacing $\Delta_{\mathrm{HFS}} = 1.8 \pm 0.1$ GHz between the peaks agreed with theoretical calculations [3]. In Fig. 3 (d), the profile of the transition $(34,33)\rightarrow(35,32)$ at 525.5 nm is shown, with a hyperfine splitting of $\Delta_{\mathrm{HFS}} = 1.5 \pm 0.1$ GHz, which also agrees with theory.

The zero-density transition frequencies ν_{exp} were thus directly measured. Experimental precisions between 7×10^{-8} and 2×10^{-7} were obtained, the highest being for the 372.6-nm transition. In Fig. 4, the frequencies are compared with the results ν_{th} of theoretical calculations [3, 5, 6], which include higher-order QED and finite nuclear-size effects. These claim an accuracy of $< 1 \times 10^{-7}$ limited by uncertainties in the three-body wave functions of states with large ($\Gamma > 10$ MHz) Auger widths; by using complex coordinate rotation methods, the precision has been improved compared to previous values. In past experiments [1], a theory-experiment difference of $|(\nu_{\mathrm{th}} - \nu_{\mathrm{exp}})/\nu_{\mathrm{exp}}| \sim (5-7) \times 10^{-7}$ was observed in the transition $(39,35)\rightarrow(38,34)$ at 597.3 nm; in the current experiment, this has been improved

to $\sim 1 \times 10^{-7}$.

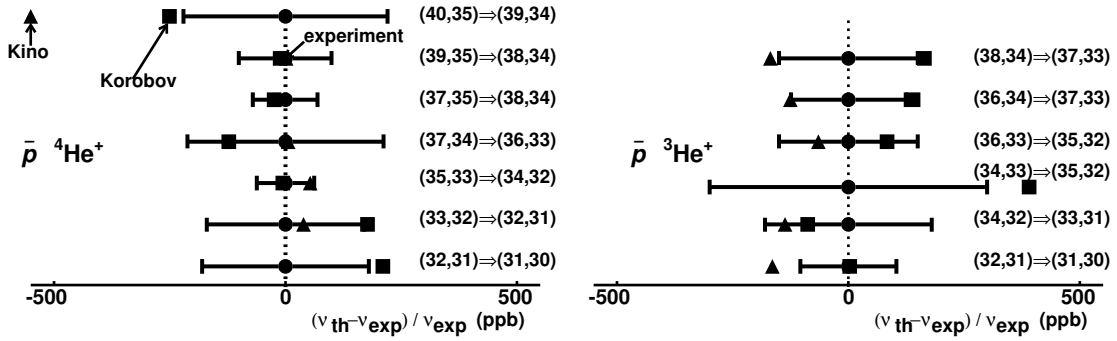

Figure 4: Comparisons between experimental (filled circles with errors) and theoretical (squares [6] and triangles [3]) transition frequencies, ν_{exp} and ν_{th}.

By comparing the experimental and theoretical frequencies, a limit δ was set on the possible difference between the antiprotonic charge ($Q_{\overline{p}}$) and mass ($M_{\overline{p}}$), and the values for the proton (Q_p, M_p). Following the method described in Refs. [1,7,8], we used the transition frequencies (which have a scale of the antiprotonic Rydberg constant $R_{\overline{p}} \propto M_{\overline{p}} Q_{\overline{p}}^2$), and the cyclotron frequency ($\omega_{\overline{p}} \propto Q_{\overline{p}} B / M_{\overline{p}}$) measured in Penning traps [9]. We found that the antiprotonic charge and mass are in agreement with the proton's to a precision of $\sim 1 \times 10^{-8}$.

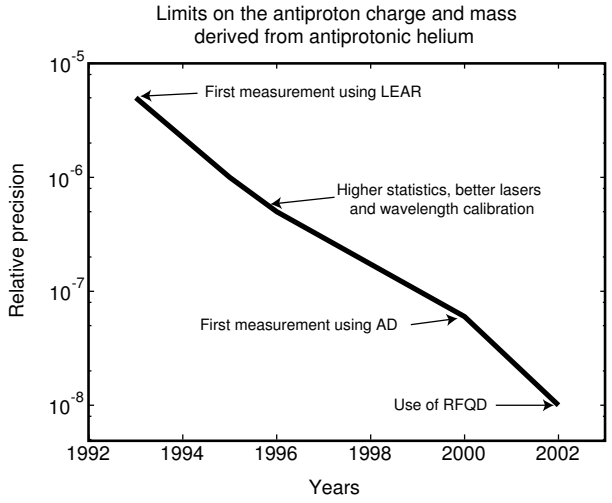

Figure 5: Relative precision on the possible differences between the antiproton mass and charge measured over the years. The results were derived by combining the results of laser spectroscopy experiments on $\overline{p}\mathrm{He}^+$ atoms, with those of Penning trap experiments by the TRAP collaboration.

In Fig. 5, the relative precisions on the possible differences between the antiproton mass and charge measured over the years are shown. These values were derived by combining the results of laser spectroscopy experiments on $\overline{p}\mathrm{He}^+$ atoms with those of Penning trap experiments by the TRAP collaboration. Further improvement of the experimental precision

requires developing higher-stability antiproton beams, new laser spectroscopic techniques, and completely upgrading the instrumentation.

1.2 Long-lived $\overline{p}\mathrm{He}^{2+}$ ions

All our past experiments dealt with the three-body $\overline{p}\mathrm{He}^{+}$ atom; in 2002, however, we observed indications of long-lived antiprotonic helium ions ($\overline{p}^4\mathrm{He}^{2+} \equiv \alpha + \overline{p}$) populating two ionic states $(n, \ell) = (31, 30)$ and $(32, 31)$ for the first time.

These ions produced in states with large principal ($n \sim 30$) and angular momentum ($\ell \sim n$) quantum numbers are theoretically expected to have microsecond-scale lifetimes, provided they are isolated in a collision-free environment. When produced in high-density targets with atomic number densities greater than $\rho \sim 10^{20}$ cm^{-3}, however, they are destroyed within picoseconds by collisional Stark effects. It was thus impossible to observe long-lived ions in past experiments carried out by ASACUSA using the 5.3-MeV antiproton beam of AD.

In 2002, we produced cold $\overline{p}\mathrm{He}^{2+}$ ions in ultra-low density targets $\rho < 10^{16}$ cm^{-3} by the following method: first, $\overline{p}^4\mathrm{He}^{+}$ atoms were formed by decelerating antiprotons using the RFQD to energies $T < 100$ keV and stopping them in an ultra-low density gas target. The atom cooled to a temperature $T = 10$ K by colliding with the surrounding helium atoms. A pulsed laser beam with a wavelength $\lambda = 470.7$ nm was used to induce atomic transitions from the metastable $\overline{p}^4\mathrm{He}^{+}$ state $(37, 34)$ to the state $(36, 33)$ having a theoretical Auger lifetime of several nanoseconds. This resulted in the atomic electron being quickly ejected, such that a $\overline{p}\mathrm{He}^{2+}$ ion occupying the state $(31, 30)$ was formed.

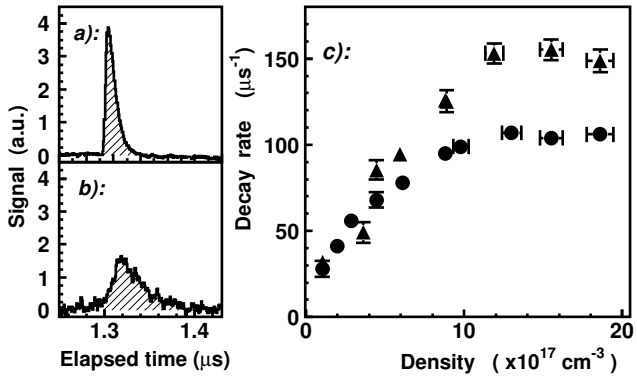

Figure 6: Laser spike of $\overline{p}^4\mathrm{He}^{+}$ transition $(37, 34) \rightarrow (36, 33)$ measured at high (a) and ultra-low (b) densities. Decay rate of this spike (filled circles), and that of the $\overline{p}^4\mathrm{He}^{+}$ transition $(39, 35) \rightarrow (38, 34)$ (triangles) at various densities.

In Fig. 6 (a), the annihilation spike observed at a target density $\rho = 5 \times 10^{21}$ cm^{-3} is shown. The spike decayed with a lifetime $\tau \sim 6$ ns. When the same transition was measured at a density $\rho = 1 \times 10^{17}$ cm^{-3}, however, the lifetime increased to $\tau_s \sim 30$ ns (Fig. 6 (b)). We also examined the annihilation spike corresponding to the $\overline{p}^4\mathrm{He}^{+}$ transition $(39, 35) \rightarrow (38, 34)$ at a wavelength of $\lambda = 597.3$ nm, and observed a similar effect.

As shown in Fig. 6 (c), the decay rates $1/\tau_s$ for the two transitions increased as a linear function of density in the region $\rho < 10^{18}$ cm^{-3}. At larger densities, however, the decay rates

saturated and remained constant, even at densities up to $\rho > 10^{21}$ cm^{-3}.

These results are consistent with the following theoretical explanation: at high densities, the decay rates of the spikes are presumably dominated by the Auger lifetime of the $\overline{p}^4\mathrm{He}^+$ resonant daughter states. At lower densities, however, the lifetimes of the $\overline{p}^4\mathrm{He}^{2+}$ ions increases, such that a prolonging of the decay rates in the annihilation spikes are observed. More experimental and theoretical studies in 2003 are necessary before we can conclude whether the above explanations are correct.

In this experiment, the collisional lifetime of a two-body exotic atom populating a specific state (n, ℓ) was measured for the first time. These values can be compared with the results of theoretical cascade calculations [10–13], which have been widely used over the last 40 years as a tool to analyze data obtained from experiments such as muon catalyzed fusion, X-ray spectroscopy, and hypernuclei production. These calculations include various effects such as radiative deexcitation, external Auger transitions, Stark transitions, Coulomb deexcitaion, and nuclear absorption during collisions. None of these effects, however, have been experimentally studied for high-n states in two-body exotic atoms before, and so the present experiment provides an important way of verifying the calculations. The experiment, moreover, deals with cold $\overline{p}\mathrm{He}^{2+}$ ions which collide with other helium atoms with low energies ($\sim$ 1 meV); the corresponding de Broglie wavelengths are so large that quantum tunneling effects may become significant.

1.3 Attempts at two-photon laser spectroscopy

In 2002, we made the first systematic attempts of two-photon laser spectroscopy of $\overline{p}\mathrm{He}^+$. All past measurements involved single-photon transitions, the experimental precision of which is limited by the Doppler broadening of the resonance lines arising from the thermal motions of the atoms. In order to improve the precision, two-photon laser spectroscopic methods may be used to diminish Doppler broadening effects. The measurement is difficult, however, because laser energies three to four orders of magnitude higher than those used in past experiments are required.

The setup of the feasibility experiment made in 2002 is shown in Fig. 7. The target consisted of a 30-mm-diam, 200-mm-long cylinder filled with helium gas at a pressure $P = 10$ Bars and temperature $T = 300$ K. We chose the room temperature condition in order to demonstrate the Doppler-cancellation feature of this method. Antiprotons with energies $T = 5.3$ MeV entered the target through a metallic window, and stopped within a volume of helium gas about $d = 8$ mm across. The $\overline{p}\mathrm{He}^+$ atoms were irradiated by two collinear ultraviolet laser beams entering through two fused silica windows. The laser beams had diameters of $d = 2$–3 mm, and extremely high energy densities ($P = 20$–50 mJ/pulse) which was necessary to induce the two-photon transition. The wavelengths were tuned to values of $\lambda = 417$ and 372 nm corresponding to the two-photon transition $(n, \ell) = (36, 34) \rightarrow (34, 32)$.

The transition was observed as shown in Fig. 8. In this experiment, the measured precision on the transition frequency 10^{-6} was in fact worse than in single-photon measurements made with the RFQD beam 10^{-7}. This was not surprising, since for these feasibility studies we used 1) a room temperature target (which resulted in increased collisional broadening), and 2) dye-laser beams at such high energy that their power and wavelength stability were impaired.

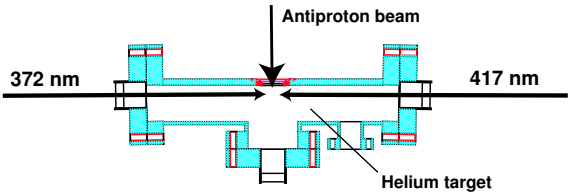

Figure 7: Setup of the experiment to study the feasibility of making two-photon laser spectroscopy of $\overline{p}\mathrm{He}^+$.

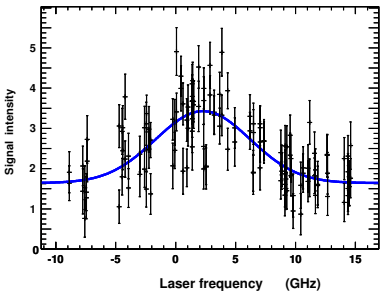

Figure 8: Profile of the two-photon resonance line $(n,\ell) = (36,34) \rightarrow (34,32)$. High-precision determination of the transition frequency was impossible, due to poor signal-to-ratio and the broad linewidth.

In order to improve the experiment and observe narrow two-photon resonance lines, i) an antiproton beam with higher stability and smaller spot-size will be necessary in order to produce $\overline{p}\mathrm{He}^+$ atoms in a smaller volume of the target (so as to reduce the laser-power requirement), ii) new laser systems with higher stabilities over longer periods of time, and narrow bandwidths are required, and iv) new experimental targets must be developed in which the $\overline{p}\mathrm{He}^+$ atoms can be irradiated by laser beams in a multi-pass configuration (this also reduces the laser power requirement). Such an improved experiment is currently being planned as a future long-term extension of the ASACUSA project.

1.4 Studies of the primary populations of $\overline{p}\mathrm{He}^+$ atoms

In 2002, we continued systematic measurements on the primary populations of $\overline{p}\mathrm{He}^+$ atoms [14], and determined the principal (n) and angular momentum (ℓ) quantum numbers of the atom's primordial (i.e., initially occupied) states. The primary populations in the states $(33,32)$, $(34,33)$, and $(35,33)$ in $\overline{p}^3\mathrm{He}$ were studied by irradiating the atom with laser pulses at various times between $t = 0.3$ and 16 μs, and measuring the intensity of the resonance spike at each timing. In this way, the population evolution $P_{(n,\ell)}(t)$ in each state was derived. The new results, when combined with data measured last year, showed that nearly all the $\overline{p}^3\mathrm{He}^+$ atoms are created in states having n-values around $n \sim 37$, confirming the conjecture [15] that the initial formation of exotic atoms occur around $n \sim \sqrt{M^*/m_e}$ (where M^* is the reduced mass of the captured particle).

1.5 Auger decay rates

The metastability of $\bar{p}\mathrm{He}^+$ is known to arise from the suppression of fast Auger decay in high angular momentum states. The Auger rate γ_A has a drastic dependence on the lowest possible transition multipolarity L, which is equal to the minimum angular momentum carried away by the Auger electron. Typically

$$\gamma_A \sim 10^{17-3L}\ \mathrm{s}^{-1} \text{ for } L = 2,3,4. \tag{1}$$

As the radiative rates (γ_r) are about 10^5–10^6 s^{-1}, states with $L \leq 3$ are Auger-dominated (so-called "short-lived") states.

By 2001, we had studied decay rates of nine $\bar{p}^4$He$^+$ states [16, 17]. Most of the states have decay rates consistent with the above approximate Eq. (1), however, we found two exceptions. One was the (37, 33) state, which was can possibly be affected by [18] an electron-excited configuration $(32, 31)_{\bar{p}} \otimes (3d)_e$ having a close level energy. Another was the (32, 31) state. Our low-density measurement with RFQD revealed that the decay rate of this state was greatly enhanced by collisions. We refer to these decay rate discrepancies 'anomalies' below [17].

In 2001 and 2002, we studied decay rates of ten more states of $\bar{p}$He$^+$, including seven states of $\bar{p}^3$He$^+$. The deduction of decay rates required different methods according to the magnitude of the rates:

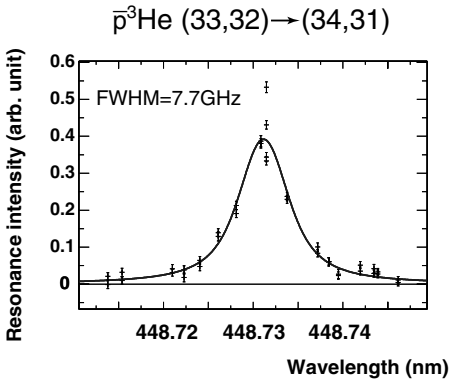

Figure 9: Wide resonances scanned for the Auger rate deduction.

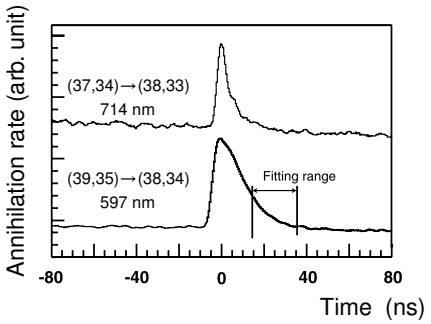

Figure 10: Prolonged laser resonance spike (lower) and not prolonged one (upper).

- Decay rates faster than 6 ns^{-1} ...wide resonances
  In this case, the resonances have much broader natural widths than the laser linewidth (3–5 GHz). Fig. 9 shows four $(n, l) \rightarrow (n-1, l-1)$ type (unfavored) wide resonances newly measured. The natural width $\Delta\nu$ were obtained by fitting the resonance curves with Voigt functions, then converted to the decay rate γ by

$$\gamma = 2\pi\Delta\nu. \tag{2}$$

- Decay rates slower than 0.1–0.2 ns^{-1} ... long tail spikes
  If the decay rates are slow enough, the laser resonance spikes appearing in the time spectra are prolonged (see Fig. 10), as the annihilations of the antiprotons delay. We can obtain the decay rates by fitting the "tails" of the spikes with exponential functions.

- Intermediate cases
  For the states that do not show either wide resonances or prolongation of the spikes, we concluded that their decay rates are between 0.1 ns^{-1} and 6 ns^{-1}.

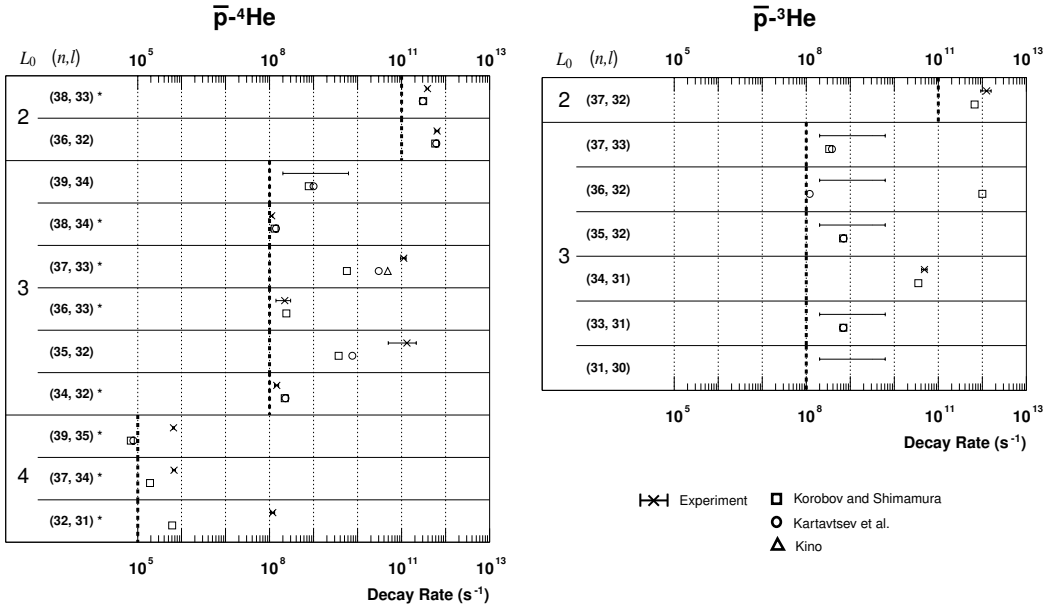

Figure 11: Experiment-theory comparison of the decay rate in logarithmic scale. The states marked with stars (*) were measured in the past experiments [16, 17]. The bold vertical dotted lines show the typical Auger rates.

Fig. 11 shows the results of our decay rate measurements of all the nineteen (including published nine) states. Theoretical values by Korobov and Shimamura [19] and Kartavtsev [18] are also plotted.

Among the latest ten results, two anomalous candidates have been found. They were the (35, 32) and (34, 31) states, which have much faster decay rates than the typical values expected by Eq. (1), and their theoretical Auger rates are also as fast as the experimental rates. These situations resemble the case of the (37, 33) state, the rate of which is assumed to be increased by state mixing with an electron-excited configuration having a close energy. The configurations $(31, 30)_{\bar{p}} \otimes (3d)_e$ for the (35, 32) state of $\bar{p}^4\mathrm{He}^+$, and $(30, 29)_{\bar{p}} \otimes (3d)_e$ for the (34, 31) state of $\bar{p}^3\mathrm{He}^+$ can have the same reason for their anomalies. For the latter case, the possibility of influence by a short-lived state was already mentioned by Kartavtsev [18].

It is also noteworthy that the decay rate of the (36,32) state of $\bar{p}^3\mathrm{He}^+$. Although one theory predicted a large anomaly, the decay rate was found not to be far from the typical value. It should be interesting to understand why difficulties were encountered in calculating this decay rate, and how to avoid them.

1.6 Quantum tunneling effects revealed in collisions with hydrogenic molecules

The lifetime of metastable states of antiprotonic helium atoms decreases when various impurity molecules (hydrogen, deuterium, oxygen, neon etc.) are mixed into the helium gas [20–23]. This quenching phenomenon is particularly interesting in the case of hydrogen and deuterium because the quenching cross section in collisions with these molecules strongly

depends on the quantum numbers n and l of the metastable states [24–27]. According to the theoretical calculations of Sauge and Valiron, an (n, l)-dependent activation barrier exists for this kind of reaction which could explain the observed quenching behaviour [28]. Their model also predicts that using a classical approach, the quenching cross section σ_q should increase with increasing temperature following the Arrhenius law:

$$\sigma_q = \sigma_0 \exp(-E_b/kT), \tag{3}$$

where σ_0 is the cross section at infinitely high temperatures (this we expect to be close to the geometrical cross section), E_b is the height of the activation barrier, k is the Boltzmann constant and T is the temperature. However, all previous measurements of quenching by hydrogen and deuterium molecules were done at 30 K, therefore, in order to test the above temperature dependence we made measurements at higher temperatures during our 2002 beamtime.

The quenching cross section of a metastable antiprotonic state can be obtained by measuring the decay rate of the state at different impurity concentrations using laser spectroscopy. Assuming that the antiprotonic helium atoms are quenched in binary collisions with the impurity molecules, the decay rate γ of the state then can be expressed as

$$\gamma = \gamma_0 + n_{\mathrm{imp}}\, v_{\mathrm{th}}\, \sigma_q, \tag{4}$$

where γ_0 is the 'intrinsic' decay rate of the state in pure helium, n_{imp} is the number density of the impurity molecules, $v_{\mathrm{th}} = \sqrt{8kT/(\pi M_{\mathrm{red}})}$ is the relative velocity of the colliding molecules [29] (where k denotes the Boltzmann constant, T the target gas temperature, and M_{red} the reduced mass of the colliding system), and σ_q is the collisional quenching cross section.

The decay rate of a metastable state can be measured using two methods. If the state can be the parent of an ordinary metastable-to-shortlived laser-induced transition, we measure the area of the laser-induced peak in the antiproton annihilation time spectrum (normalized to the total background) at different laser firing times as seen in Fig. 12. Since the area of the peak is proportional to the population of the parent state at the time of the laser firing, this way we obtain the population lifetime τ_p of the parent state. If feeding to this state from upper states is negligible, then the inverse of this lifetime is equal to the decay rate of the state: $\gamma = 1/\tau_p$. This is the 't1-scan' method [30].

If the state is not accessible with an ordinary laser-induced transition, the HAIR (hydrogen-assisted inverse resonance) or DAIR (deuterium-assisted inverse resonance) methods can be used [27,31]. The principle of these methods is that higher-lying (larger-n) metastable states are quenched more strongly in collisions with hydrogen or deuterium molecules than lower-lying ones, therefore if we add a suitably chosen quantity of hydrogen or deuterium to the helium gas, this can turn a normally long-lived state into a short-lived one, while retaining the longevity of an adjacent lower-lying state. It is then possible to induce a laser transition from the lower-lying state to the upper-lying one ('inverse resonance'). The inverse of the lifetime τ of the laser-induced peak is equal to the decay rate of the daughter state: $\gamma = 1/\tau$, even if there is feeding from upper states. The lifetime of the peak can be obtained by fitting a theoretical function [27] to a part of the annihilation spectrum that contains the peak (see Fig. 13). However the intensity of the laser-induced peak decreases drastically at

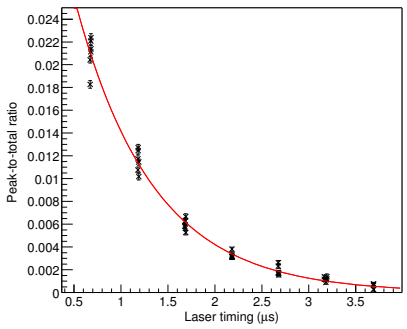

Figure 12: 'T1-scan' (see text) of the transition $(37, 34) \rightarrow (36, 33)$ measured at 300 K, 8 bar and deuterium concentration of 30 ppm. The solid line shows the fit of an exponential function with lifetime τ_p.

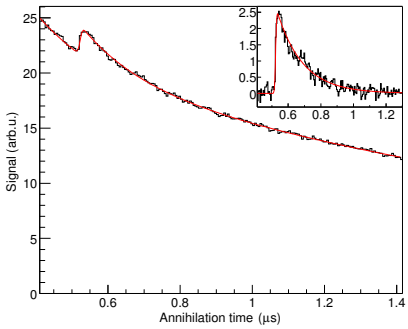

Figure 13: Summed-up antiproton annihilation time spectrum of the transition $(37, 36) \rightarrow (38, 37)$ measured at 25 K, 1 bar and deuterium concentration of 10000 ppm. This spectrum was obtained by adding 15 annihilation time spectra together. The solid line represents the result of fitting a function [27] to determine the lifetime of the laser-induced peak. The inset shows an enlarged view of the peak with the fitted background subtracted.

high temperatures, making the HAIR/DAIR method impossible to use above 100K. Even at lower temperatures, 10-15 AD shots had to be collected and added together to improve the quality of the peak.

Six 8-hour shifts were used for measuring the quenching cross sections of three metastable antiprotonic states with hydrogen and deuterium impurity gases at different temperatures. The measurements at 300 K were done using the two-photon target chamber while the measurements at lower temperatures were done using our standard cryostat. The number density n_{imp} of the impurity molecules was varied by either changing the concentration of the impurity molecules or changing the pressure of the target gas. An example of fitting Eq. (4) to the obtained data is shown in Fig. 14. Table 1 shows the summary of these measurements. The results, together with previous measurements at 30 K, clearly show that the quenching cross sections indeed increase with increasing temperature. Unfortunately, we only had time to study the temperature dependence of the state $(38, 37)$ with deuterium in detail. If we plot the logarithm of the quenching cross section σ_q versus the inverse temperature $1/T$, the Arrhenius law [Eq. (3)] will result in a straight line. Fig. 15 shows the collected data on such a plot; a deviation from the Arrhenius law is clearly visible. Thus we fitted a function to the experimental data which is a sum of an exponential and a constant:

$$\sigma_q = \sigma_0 \exp(-E_b/kT) + \sigma_t, \tag{5}$$

where σ_t is independent of the temperature. This term is most likely related to the quantum tunneling of the colliding deuterium molecule through the activation barrier, as suggested by Sauge and Valiron. From the fit, we obtained the following preliminary values: $E_b =$

(0.015 ± 0.002) eV, $\sigma_0 = (5.3 \pm 2.1) \times 10^{-16}$ cm^2, $\sigma_t = (0.34 \pm 0.01) \times 10^{-16}$ cm^2. For comparison, the geometrical cross section of the D_2–He collision is 21×10^{-16} cm^2 [32, 33], which is significantly larger than the measured σ_0. This difference is also predicted by Sauge and Valiron; according to their calculations, quenching of the metastable states by hydrogen molecules at low temperatures (~ 30 K) is predominantly caused by ortho-$H_2(J=1, m_J=0)$. Since molecular hydrogen has four species – one para-$H_2(J=0, m_J=0)$ and three ortho-$H_2(J=1, m_J=\pm1, 0)$ – and these are equally populated, the measured σ_0 should be 1/4 of the geometrical cross section; in other words, the steric factor of this reaction is 1/4. On the other hand, molecular deuterium has nine species: one ortho-$D_2(J=0, m_J=0)$, three para-$D_2(J=1, m_J=\pm1, 0)$ and five ortho-$D_2(J=2, m_J=\pm2, \pm1, 0)$ but unfortunately no theoretical calculations have been made to determine which deuterium species dominate the quenching mechanism at low temperatures.

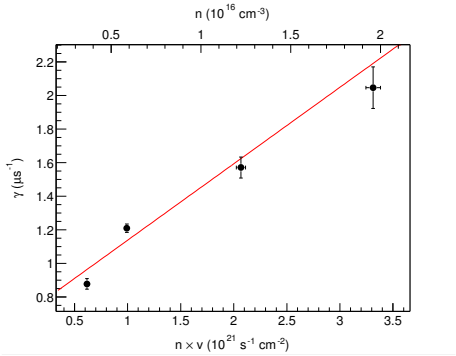

Figure 14: Decay rate of the state $(37, 34)$ versus the flux $n_{\mathrm{imp}} \times v_{\mathrm{th}}$ measured at 300 K with deuterium. The top axis shows the approximate number density of D_2 molecules. The solid line represents the result of fitting Eq. (4) to the experimental data.

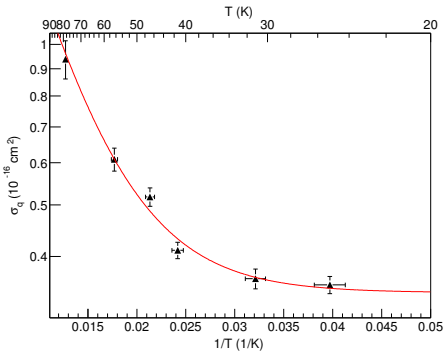

Figure 15: Quenching cross section of the the state $(38, 37)$ in collisions with deuterium molecules versus the inverse temperature. Note the logarithmic scale of the vertical axis. The result of fitting Eq. (5) to the data is also shown.

These measurements, together with the theoretical calculations, can give us a better understanding of the physico-chemistry of cold interstellar and protostellar clouds where similar low temperature reactions play a significant role, especially various hydrogen/deuterium fractionation processes that cause enrichment of deuterium in these environments.

2 Development of an ultra-slow antiproton beam

ASACUSA is preparing an ultra-slow monoenergetic antiproton beam by sequentially combining the beams from the AD (down to 5.3 MeV), the RFQD (Radio-Frequency Quadrupole Decelerator; down to 50–100 keV), and confining them in a MRT (multi-ring electrode trap [34, 35]) installed in a superconducting magnet of 5 T. Here they are cooled and compressed before being extracted, reaccelerated to eV-scale energies and delivered via a beam transport line to gas or solid targets. The MRT, the superconducting solenoid and eV-beam transport line are jointly known as "MUSASHI", or the Monoenergetic Ultra-Slow Antipro-

Table 1: Summary of the impurity measurements in 2002. All values are preliminary.

State (n, l)	Impurity gas	Temperature (K)	Method	σ_q (10^{-16} cm^2)
$(37, 34)$	hydrogen	300	t1-scan	4.27±0.35
$(37, 34)$	hydrogen	100	t1-scan	1.93±0.08
$(37, 34)$	deuterium	300	t1-scan	4.55±0.37
$(37, 34)$	deuterium	100	t1-scan	1.55±0.04
$(38, 35)$	hydrogen	60	HAIR	5.82±0.41
$(38, 35)$	deuterium	60	DAIR	5.32±0.35
$(38, 35)$	deuterium	30	DAIR	4.02±0.16
$(38, 37)$	hydrogen	60	HAIR	0.97±0.06
$(38, 37)$	deuterium	75	DAIR	0.94±0.08
$(38, 37)$	deuterium	60	DAIR	0.61±0.03
$(38, 37)$	deuterium	48	DAIR	0.52±0.02
$(38, 37)$	deuterium	40	DAIR	0.41±0.01
$(38, 37)$	deuterium	30	DAIR	0.36±0.02
$(38, 37)$	deuterium	25	DAIR	0.35±0.01

ton Source for High-precision Investigations. MUSASHI will open a new research field of collision dynamics to be studied in processes like antiprotonic atom formation and ionization processes under 'single collision conditions'.

During 2002, we successfully trapped and stacked of the order of 10^6 antiprotons in the trap. Antiprotons were then cooled and radially compressed, and were extracted from the trap. Approximately 10,000 antiprotons per 'cycle' (= typically 1 or 2 AD shots) reached the end of the beam line at 250 eV.

Since the 'single collision' experiments require an order of magnitude more antiprotons, most of the beam time was spent to improve the extraction efficiency. We have identified possible sources of the problem, as discussed below. Efforts to improve the extraction efficiency will continue in 2003.

2.1 Trapping and stacking of millions of antiprotons

For an efficient and stable trapping, an ultra-high vacuum of better than 10^{-12} Torr at the trap volume is an essential factor. The temperature of the bore tube in which the trap electrodes reside therefore had to be stable at 5 K, in order to freeze out any possible residual gases. We observed a clear shortening of trapping time when the temperature exceeded 10 K.

The total number of trapped antiprotons were estimated from the number of antiproton annihilations detected by the track detectors (scintillator bars placed along side the trap and the extraction beam line, as described in the ASACUSA 2001 status report), taking into account their effective solid angle calculated with GEANT simulations. Since the counting rate of antiproton annihilation at the time of the extraction was more than that handled by the DAQ system, the correct number was evaluated by the scalers installed. After careful optimization of the trapping parameters, we achieved trapping of 2 million antiprotons per

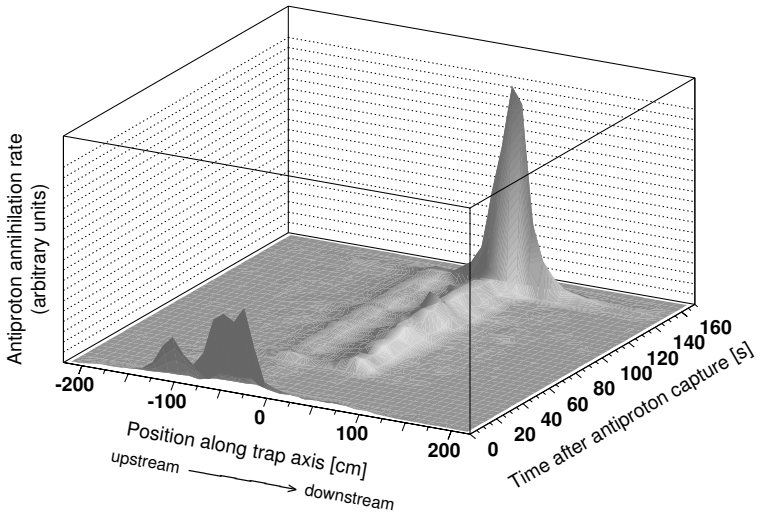

Figure 16: Observed annihilation rate of antiprotons are plotted vertically as a function of time and position along the trap axis. Numerous annihilations occurred for the first 5 seconds during the cooling process and a small number during trapping. During the extraction at 150–160 s, the major part of antiprotons annihilated downstream.

AD shot and 50% of them, i.e., 1 million were cooled to less than an electronvolt and stayed stably in the harmonic potential until the end of our running cycle of 100–200 seconds (see Fig. 16).

We were able to trap some five million antiprotons by stacking five successive AD shots without loss. The stacking did not seem to work better for more than 6 shots, for some reason which we have not understood yet, as trapped antiprotons started to annihilate inside during the cycle. Theoretically our MRT should be able to accommodate many more antiprotons, and we hope to improve the conditions so as to be able to stack large numbers of antiprotons in 2003.

2.2 Cooling of antiprotons and compression of the antiproton cloud

2.2.1 First observation of electron plasma excitation and relaxation by antiproton injection

Diagnosis of electron plasma in the harmonic trap potential is very important for effective cooling of antiprotons from several keV down to less than an electronvolt. This year, we successfully measured several plasma excitation modes up to (7,0), which gave information on the density, shape and temperature of the electron plasma. Fig. 17 shows the resonance frequency variation of the (1,0), (2,0) and (3,0) modes after antiproton injection, which manifests the temperature of antiprotons in the trap. It can be used as a sensitive real-time monitor of the plasma. The observed evolution of the mode frequency is qualitatively in accordance with our simulation. This is the first successful measurement ever done using a trap of two different particles with the same charge, which is expected to provide useful information in the field of non-neutral plasma physics.

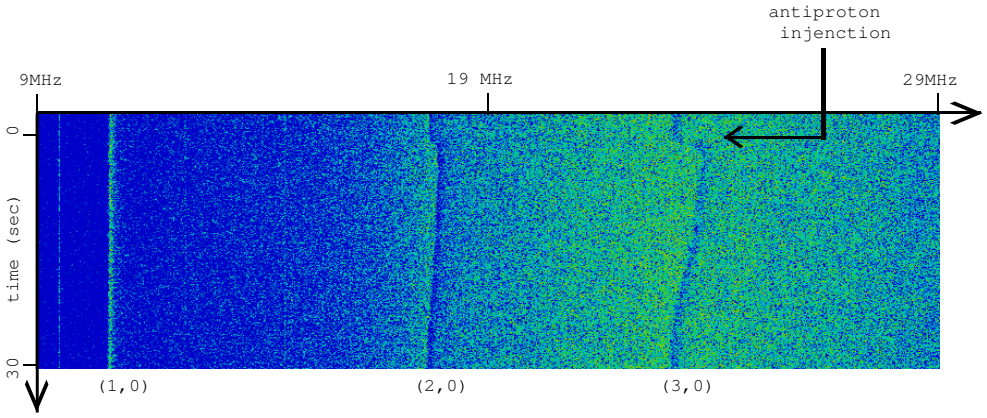

Figure 17: The two-dimensional display of the spectrum analyzer output shows the response of electron plasma when 2 million antiprotons were injected. The resonance frequencies are plotted in the horizontal axis. Time evolution of the three azimuthally symmetric plasma modes (1,0), (2,0) and (3,0), excited by wide-band noise at 20 mV_{pp}, is shown in vertical direction downwards.

2.2.2 Cooling and compression

After some 30 seconds the antiprotons were sufficiently cooled by the electrons. The final temperature of the antiproton cloud was evaluated by measuring antiproton annihilation while gradually ramping-down one side of the trap potential. The electrons were then kicked out of the MRT by opening the trap potential for a short enough period for the antiproton to stay, but long enough for the electron to escape. Rectangular pulses of 550 ns width were applied to the electrodes to open the trapping potential. Applying this method a few times, the number of electrons became orders of magnitude smaller, small enough to be neglected, while keeping all the antiprotons in the potential.

After electron kick-out, we applied an RF field to one of the trap electrodes segmented azimuthally in 4 parts for radial compression of the antiproton cloud, which is essential for efficient extraction of cooled beams out of the strong magnetic field. According to simulations, the cloud radius has to be smaller than 1 mm in the magnet because otherwise the beam would expand to more than 2 cm at the exit of the magnet and cannot be transported.

We tried two types of compression: a) sideband cooling and b) plasma rotation. Sideband cooling is a technique to cool the otherwize semi-unstable magnetron motion by coupling it to the axial motion of the cloud via an RF field with the sum frequency of the two motions. In our trap of 50 V depth, the sum frequency for antiproton was around $\nu_s \sim 250$ kHz. We spent a significant part of our beam time on measurements with different sideband frequencies, fixed or swept, or with wide-band RF, at various strengths of the fields. We observed that the RF field was effective in preserving the size of the cloud for a typical period of 100 seconds of its application; without the field the cloud seemed to expand gradually. We also observed some enhancement in the number of extracted antiprotons around 240 kHz, but the resonance was broader than 10 kHz in contrast to 2 kHz for tests with protons or H_3^+ ions and the effect was not so prominent. This may be due to the fact that the antiprotons initially had a large diameter of 1 cm FWHM when captured, because of a large emittance

and longitudinal momentum bite of the incident beam from the AD and the RFQD (see section 2.4.1.

Another compression method, the plasma rotation is a technique to spin up the rigid rotation of the antiproton plasma by an azimuthally rotating RF field applied to the segmented electrode. This method requires the density of the cloud to be large enough so that the cloud acts as a plasma. We therefore tested compression of two-component plasma, i.e. the 10^6-antiproton cloud with 10^8 electrons trapped simultaneously. This, however, resulted in decrease of the number of antiprotons on the center of axis, probably because the antiprotons were pushed away while the electrons were compressed radially. Therefore antiprotons must be compressed after electron kick-out. Our various attempts at different frequencies and voltages did not work out even when the number of antiprotons was increased by stacking.

2.3 Extraction of 250 eV antiprotons

Our extraction beamline was designed for transport of ultra-slow antiprotons extracted from the MRT at variable energies between 10 and 1500 eV [36]. We chose the beam energy of 250 eV for optimum transport. The beam was sharply focused 3 times by two Einzel lenses and one asymmetric lens, where variable apertures were installed for differential pumping of 6 orders of magnitude in vacuum pressure. Two types of beam profile monitors have been developed for diagnostic purpose in the beamline: we used two sets of an MCP (multichannel plate) combined with a delay-line position sensitive detector (MCP-PSD), and a multiwire detector for non-destructive measurement of the beam.

The MCP-PSD was sensitive enough to allow single counting of each antiproton, giving two-dimensional images of ultra-slow antiproton beams. To make sure that the image corresponded to real antiprotons and to remove possible signals from other particles like electrons and H^- ions and from decay of radioactive nuclei created by antiproton irradiation, we prepared two scintillation counters around the MCP detector for coincidence measurement. Only signals from antiproton annihilation can trigger both detectors at the same time, so that a pure image of antiproton beams can be available.

We detected 10,000 antiprotons per cycle at 250 eV by the MCP-PSD downstream, extracted as a continuous monoenergetic beam for a prolonged period of 5 seconds by successful application of exponential ramping of the trapping potential. Fig. 18 shows a 2-dimensional plot of the spatial distribution of the beam detected by the MCP-PSD after the first focus point.

2.4 Efforts to improve the extraction efficiency from the trap

Although 250-eV antiprotons were successfully extracted from the trap, the extraction efficiency was quite low. A large fraction of antiprotons hit the extractors at the exit of the field and only a small fraction was extracted. This is probably due to the insufficient compression of the antiproton cloud in the trap, which in turn is due to the large radial distribution of the incident antiproton beam (injected into the trap from the RFQD).

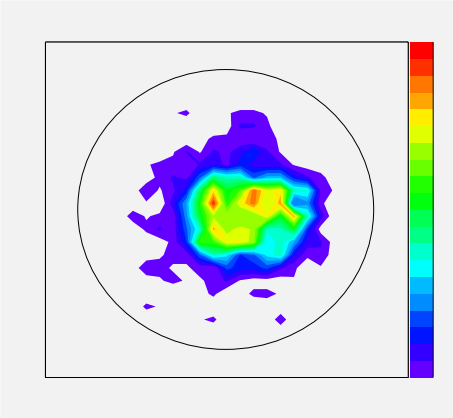

Figure 18: A two-dimensional image of the ultra-slow antiproton beam extracted at 250 eV, detected by an MCP-PSD placed after the first focusing point with an aperture with 1-cm diameter opening. The circle represents the size of the effective area of the MCP which was 2 cm in diameter. The total count of antiproton was 10,000 per cycle.

2.4.1 Diagnosis of beam transport into the trap

In order to actually measure the beam spot size at the entrance of the trap, we developed and installed two sets of special thin-foil beam profile monitor at the entrance of the multi-ring trap. The foils also served as a vacuum isolator between the low energy beam transport (LEBT) and the MRT.

An example of the detected antiproton beam profile measured is shown in Fig. 19. In spite of our efforts, the beam at the foil detector had a distribution of 1 cm FWHM even at the best tuning conditions, which was 5–6 times larger than the design value. This we believe is the reason for the low extraction efficiency from the trap.

2.4.2 Circumstantial evidences

So far, we have not yet identified the reason for the large beam spot size observed at the entrance of the MRT, but there are the following circumstantial evidences which may relate the low extraction efficiency to the (larger-than-expected) AD beam emittance and energy spread.

- The deceleration efficiency of the RFQD was typically 25%, in contrast to 40% for protons measured at tandem accelerator at Aarhus University. Lower efficiency for antiprotons can be attributed to the wide energy spread of the antiproton beam from the AD beyond the acceptance of the RFQD.
- We obtained slightly better results with long bunches of 200 ns where the beam emittance is better, instead of short-bunches of 90 ns (2σ).
- The deceleration efficiency of the RFQD had a broad and weak dependence on the phase tuning of the RFQ buncher, and the number of antiprotons captured in the 10-keV potential after the degrader foil did not change sharply when the beam transport energy was changed around 100 keV.

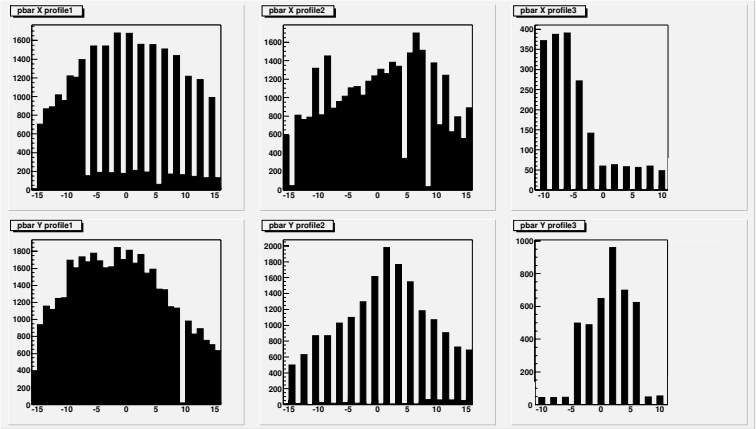

Figure 19: Two-dimensional (X and Y) profiles of the 110 keV antiproton beam after the RFQD, incident into the superconducting solenoid of the trap, were diagnosed by two multi-wire secondary-electron emission detectors (profile 1 & 2) and the foil beam profile monitor (profile 3). The signal strength from each wire or strip electrode of the detector is plotted in arbitrary scales against the beam position shown in millimeter unit.

3 Stopping power measurements

The measurements with the ESA (electrostatic analyser) apparatus were continued in 2002 during 3 weeks (including setting-up). The apparatus consists of two ESA's, one before the target selecting a narrow energy slice of the beam from the RFQD, and one after the target measuring the exit energy [37]. The main problem experienced in 2001 was the strongly varying intensity from the AD from shot to shot [38], and this was cured from the machine side from the start of 2002. In addition we had installed our own normalisation counters for the run in 2002. This led to much nicer scanning profiles, and as a result much more accurate determinations of stopping powers. An example of an exit-energy scan for antiprotons traversing a 250 A aluminium foil is shown in Fig. 20.

In 2002 stopping powers of aluminium, nickel, gold and lithium fluoride were measured in the energy range between 1 keV and 70 keV. As an example, we show in Fig. 21 the results for aluminium. The much higher quality of the data is apparent, and more detailed comparisons with theories are possible, e.g. with the free-electron gas model [39] and the binary stopping theory [40]. The thickness of the aluminium foil is known roughly from the production process, but a fine adjustment of the foil thickness has been made by scaling our measurements with protons on the same foil to the recommended proton stopping power curve [41]. One issue in low-energy stopping is the applicability of the free-electron gas approximation, which leads to a velocity-proportional stopping power. It has been established by our previous measurements [38], that this approximation is valid for metallic targets and carbon. This is, however, not expected for insulator targets. We have investigated this question by measurements of the stopping power of a large band-gap insulator, LiF. The preliminary results are shown in Fig. 22. Although the velocity dependence can be extracted from the data, and it is surprisingly close to being velocity-proportional, it is evident that there is a problem with the thickness. A re-normalisation to the ICRU curve [41] is a possibility.

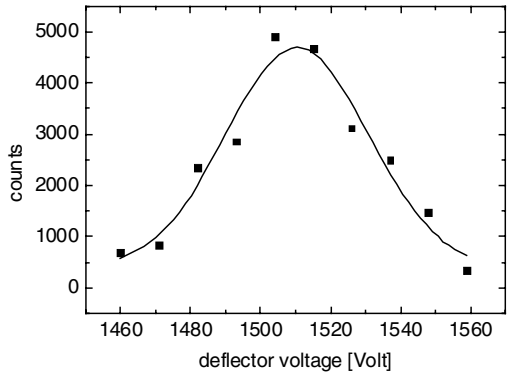

Figure 20: Deflector-voltage scan for a 6-keV antiproton measurement on aluminium from the 2002 run.

However, in this case we believe that our proton results are more accurate than the data on which the ICRU-curve is based. Also the measurements from Linz [42] are at variance with this ICRU curve. This problem will be addressed by alternative thickness determinations than that from the production process. In addition, independent measurements in Linz and in Aarhus on similar foils would be interesting.

4 Ionization apparatus

Aiming to measure ionization cross sections of various targets in the keV-energy region, we have designed and constructed an apparatus where antiprotons with energies lower than 1 keV from the antiproton catching trap will be accelerated up to 20 keV at the entrance. The apparatus consists of four chambers as shown in Fig. 23, which are separately evacuated.

Acceleration occurs at the potential gap between the GND chamber and the Collision chamber. Antiprotons then collide with an effusive target gas (D, D_2, He, Ne, Ar, Xe, etc.). The created target ions are extracted through a flight tube onto a micro channelplate detector (IONMCP), and the charge-to-mass ratio of the ions is identified by measuring their time-of-flight. The projectile antiprotons are detected by another MCP (PROJMCP). See Fig. 24 for details.

In Fig. 25 other components in the Collision chamber are shown. Effusive gases come through a skimmer from the Source chamber, then pass through the collision centre and enter into the Dump chamber for differential pumping.

The target thickness together with the detector efficiency is determined in advance by a similar measurement using a keV electron beam and applying well-established electron impact ionization cross sections. In this case the Faraday cup is used for the normalization instead of PROJMCP.

Required densities of the order of 10^{10}–$10^{11}/\mathrm{cm}^3$ are obtained for He, Ne, Ar while keeping the base pressure low enough for the detector operation and for the connection to the

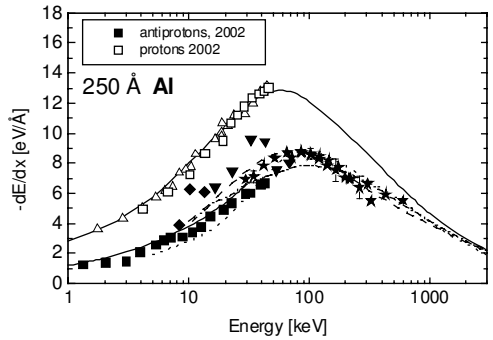

Figure 21: Measurements of the stopping power of aluminium for protons and antiprotons. The measurements performed in 2002 are shown as squares; open squares are for protons and filled for antiprotons. The full-drawn curve is a recommended proton stopping power, and the other curves represent various calculations for antiprotons.

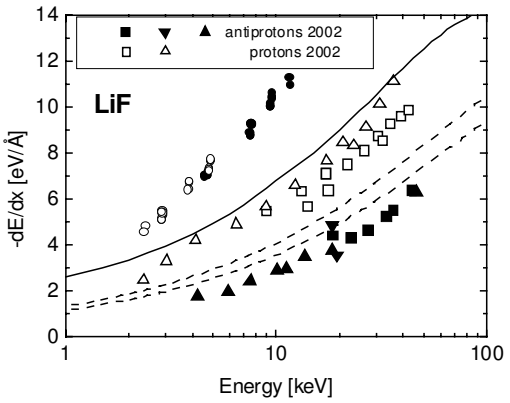

Figure 22: Measurements of the stopping power of lithium fluoride. The 2002 measurements are shown with triangles and squares; the open triangles and squares are for protons and the filled squares and triangles are for antiprotons. The filled and open circles are proton measurements from [42]. The upper curve is a recommended curve for protons [41], whereas the lower curves are calculations for antiprotons from the binary stopping theory [40].

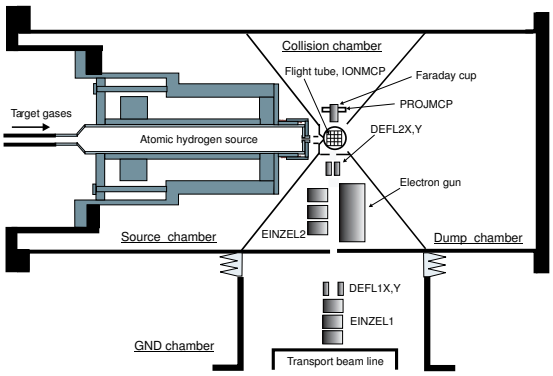

Figure 23: Schematic drawing of the ionization apparatus. The electron gun and the second Einzel lens (EINZEL2) are on a linear feedthrough so that each of them can be on the beam axis. The Faraday cup and the MCP for projectile antiprotons (PROJEMCP) are also interchangeable.

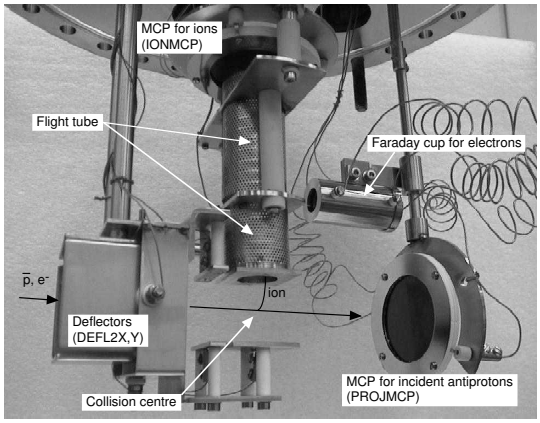

Figure 24: Side view of the detection part.

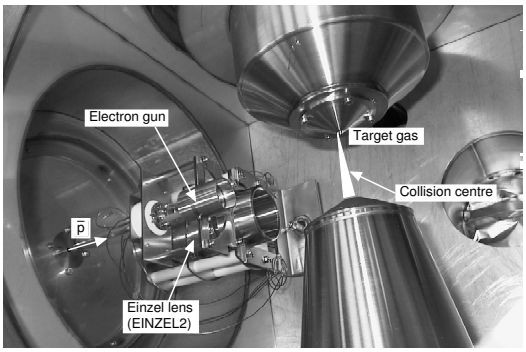

Figure 25: Inside of the collision chamber.

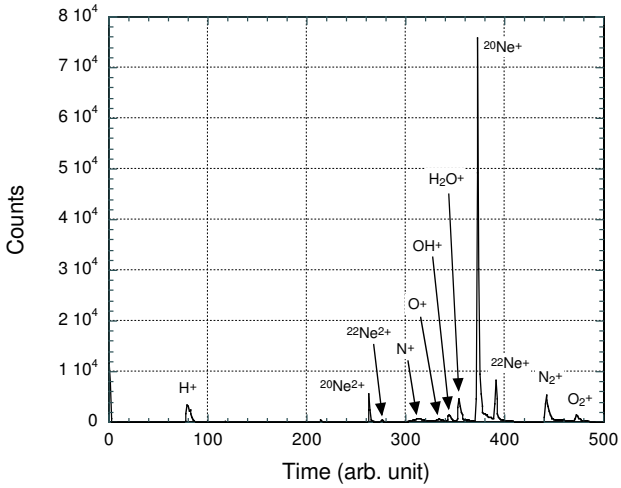

Figure 26: An Example of the TOF spectrum. Ne gas was introduced as a target.

extraction beamline. Fig. 26 shows a TOF spectrum of Ne and residual gases. Pulsed electron beams (3 keV; approximately 30 ns width) were used and we can see that the isotopes of Ne are clearly separated. Preparation of the atomic deutrium beam is in its final stage. The density is yet to be measured, but the source is in operation. Construction of a flammable gas handling system compatible with CERN safety regulation is underway.

In conclusion, the ionization apparatus is ready for measurements and awaits the further development of the technique for extraction from the trap. In this respect, we need 10^6 extracted antiprotons per AD shot for measurements of the cross sections for single ionization of atomic deuterium, a few times 10^5 per shot for D_2, He, Ne and about 5×10^4 for Ar, Xe.

Part II
ASACUSA Plans for 2003

1 Search for long-lived $\overline{p}p$ atoms

In 2003, we will attempt to observe long-lived antiprotonic hydrogen ($\overline{p}p$) atoms; these are two-body Coulomb systems composed of a proton and antiproton. The measurements will be made by decelerating antiprotons to energies $T \sim 30$ keV using the RFQD and achromatic beamline commissioned this year, and stopping them in an ultra-low density hydrogen target. Theoretical calculations show that the $\overline{p}p$ atom should be initially formed in states with n-values of around 25, and have mean lifetimes $\tau = 10$–100 ns at the target densities used here.

If the atoms are indeed formed in the expected n-region and have relatively long lifetimes, it should be possible to carry out laser spectroscopy of the atom. Ultraviolet laser beams at wavelengths of $\lambda = 250$–350 nm will be used to deexcite the antiprotons occuping the $n = 25$ states, to states with $n = 21$. It is theoretically expected that the mean lifetime of the $\overline{p}p$ would then decrease by about 10–20%, and that this can be detected as a change in the shape of the delayed annihilation time spectrum. Such experiments will be attempted next year, provided that long-lived $\overline{p}p$ atoms are successfully observed.

2 Spectroscopy of Antiprotonic Helium

2.1 Development for future two-photon laser spectroscopy experiments

We intend to continue developmental work for future two-photon laser spectroscopy experiments of $\overline{p}\mathrm{He}^+$ atoms. Although we do not expect that the experimental precision on the transition frequencies (and thus the limit on any possible difference between the antiproton and proton masses and charges) will be improved in 2003 due to the technological difficulties involved, we hope to validate several experimental techniques needed for future higher-precision experiments. As a first step, we will attempt two-photon laser spectroscopy measurements using helium targets of much lower density compared to those used in 2002, thus decreasing collisional broadening effects (see above). The measurement will be made by using the RFQD to decelerate antiprotons to $T = 60$ keV, and stopping them in a helium target at an atomic density of $\rho \sim 10^{17}$ cm^{-3}. The $\overline{p}\mathrm{He}^+$ atoms are expected to form in a much larger volume of helium gas (diameter $d = 30$ mm) compared to the experiments made in 2002 ($d \sim 5$ mm) so that larger laser powers would be needed to irradiate all the atoms and induce the two-photon transition. Targets having specially-shaped laser mirrors are now being designed, so that the $\overline{p}\mathrm{He}^+$ atoms will be irradiated efficiently by the lasers.

2.2 Systematic studies of $\overline{p}\mathrm{He}^{2+}$ ions

We plan to make systematic studies of both $\overline{p}^3\mathrm{He}^{2+}$ and $\overline{p}^4\mathrm{He}^{2+}$ ions using the RFQD, in order to determine whether the anomalies observed in the delayed annihilation time spectrum in 2002 (see above) was caused by long-lived ions. Many ionic states over a larger range of n-values will be studied, as well as ions created after Auger emission from $\overline{p}\mathrm{He}^{+}$ states having extremely short ($\tau = 100$-ps) Auger lifetimes. To carry out these experiments, we plan to develop new Cherenkov detectors with faster response speeds.

2.3 Measurements of the higher-lying states of $\overline{p}\mathrm{He}^{+}$ atoms

So far, all our laser spectroscopic studies involved $\overline{p}\mathrm{He}^{+}$ states having n-values less than 40. Although many more metastable states are predicted to exist in the $n > 40$ regions, they have never been observed because no antiprotons seem to populate them. In 2003, we intend to use the RFQD to produce $\overline{p}\mathrm{He}^{+}$ atoms in ultra-low density targets, where it is hoped that these higher-lying states would retain their populations. An optical parametric amplifier will be used to produce intense infrared laser beams, and study the higher-lying transitions. These measurements and the physics motivation have already been fully described in the ASACUSA proposal [43].

2.4 Systematic studies of quantum tunneling effects in collisions with hydrogenic molecules

- Quenching of the state $(38, 37)$ by deuterium at low temperatures were measured in 2002. We plan to repeat these measurements with hydrogen to reveal any isotope effect.

- The model of Sauge and Valiron suggests that at low temperatures quenching is predominantly caused by quantum tunneling; at medium temperatures by quantum tunnelling and classical quenching by some of the ortho/para hydrogen/deuterium species; at high temperatures by quantum tunneling and classical quenching by all the ortho/para hydrogen/deuterium species. To test this prediction, we need detailed data in a broad temperature range. In 2002, quenching cross sections of the state $(37, 34)$ were measured with hydrogen and deuterium at 100 and 300 K; therefore in 2003 we plan to make similar measurements at several temperatures around 25–75 K. (Quenching cross sections of this state with hydrogen and deuterium were measured previously at LEAR at 30 K but we need more temperature points.)

- We plan to make the same experiments with the state $(39, 35)$ as with the state $(37, 34)$ to see how states with different (n, l) behave.

- Depending on the time available, we plan to investigate the temperature dependence of as many other states as possible.

2.5 Study of the hyperfine structure of antiprotonic helium

In 2001 we succeeded in the first measurement of microwave-induced hyperfine transitions in the $(n, L) = (37, 35)$ state of antiprotonic helium with a relative precision of 3×10^{-5} [44]. The values agree with recent theoretical calculations [45–47] on a level of 6×10^{-5}, which roughly corresponds to the estimated theoretical accuracy. The hyperfine structure (HFS) of $\overline{\mathrm{p}}\mathrm{He}^+$ is a consequence of the interaction of the magnetic moments of the electron and the antiproton, and is very unique due to the large angular momentum $\vec{L}_{\overline{p}}$ of the antiproton. The experiment has fully confirmed the presence of a quadruplet structure originating from the hyperfine coupling of $\vec{L}_{\overline{p}}$, the electron spin $\vec{S}_e$, and the antiproton spin $\vec{S}_{\overline{p}}$, as predicted by Bakalov and Korobov [45] (cf. Fig. 27 (left)). Due to the large angular momentum of the antiproton, the dominant splitting arises from the interaction of the electron spin $\vec{S}_e$ and the antiproton angular moment $\vec{L}_{\overline{p}}$. This leads to a doublet which we call *hyperfine (HF)* splitting with $\vec{F} = \vec{L}_{\overline{p}} + \vec{S}_e$. The interaction of the $\overline{\mathrm{p}}$ spin magnetic moment with the other magnetic moments splits each sublevel F^+ and F^- into a still finer doublet classified by the total angular momentum $\vec{J} = \vec{F} + \vec{S}_{\overline{p}}$. We refer to this as *superhyperfine (SHF)* splitting.

The measured microwave resonance frequencies, ν^+_{HF} and ν^-_{HF}, are primarily sensitive to the $\overline{\mathrm{p}}$ *orbital* magnetic moment, and constitute a first measurement of the orbital g-factor for either proton or antiproton with an accuracy of 6×10^{-5}. On the other hand, the splitting between ν^+_{HF} and ν^-_{HF} is caused by the $\overline{\mathrm{p}}$ spin magnetic moment $\vec{\mu}_{\overline{p}}$ which is currently known with a precision of 0.3% [48]. The experimental error on $\nu^+_{\mathrm{HF}} - \nu^-_{\mathrm{HF}}$ is much larger that the precision on each frequency, yielding a value for $\vec{\mu}_{\overline{p}}$ with an error of 1.6%. The theoretical precision for $\nu^-_{\mathrm{HF}} - \nu^+_{\mathrm{HF}}$ is the same as for each value separately (5×10^{-5}), so that no new calculations are needed if the experimental precision could be improved. For that, it will be necessary to reduce the experimental line width. The measured line width $\gamma_{\mathrm{exp}} = 5.3 \pm 0.7$ MHz is larger than the estimated experimental resolution of 1 MHz. This can come either from collisions, the inhomogeneity of the magnetic field over the stopping distribution of $\overline{\mathrm{p}}$, a residual constant magnetic field inside the cryostat, or the fact that the many substates

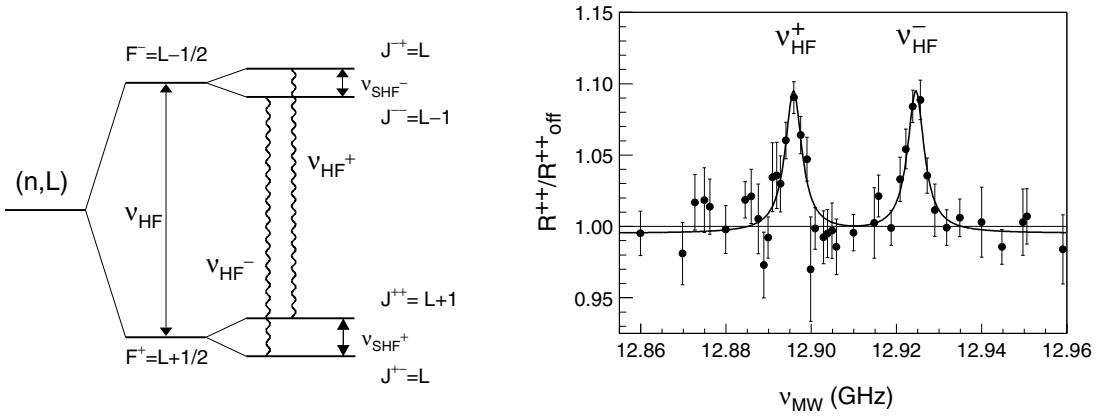

Figure 27: Left: Schematic view of the HF and SHF splitting of a $\overline{\mathrm{p}}\mathrm{He}^+$ state. Wavy lines denote allowed magnetic transitions associated with an electron spin flip. Right: Microwave scan showing clearly two resonance lines at the predicted frequencies. The width of the lines of ~ 5 MHz corresponds to 4×10^{-4} of the central frequency.

with magnetic quantum numbers $m = -J \ldots J$ each have different Rabi frequencies.

In 2001 we already measured at two different densities, but with the limited statistics, we could not observe a significant dependence of the line width on the target density. Theoretical calculations by Korenman [49] and Bakalov [50] agree that the shift of the line centres with density is very small, but disagree on the collisional broadening at our densities. While Bakalov predicts it to be or as small as 10 kHz [50], Korenman estimates that the shift can be of the order of MHz [49]. In order to test this and to possible reduce the linewidth, we plan to do systematic measurements at different densities with improved statistics. The current data were taken within 5 shifts, and we plan to take 4 weeks of data in 2003. We will also improve the absolute accuracy of our microwave frequency source below the current level of $(9 \pm 2) \times 10^{-6}$ by using an external 10 MHz reference signal with atomic clock precision that is available at the AD.

3 Experiments using the ultra-slow antiproton beam

3.1 Improvement of the antiproton extraction efficiency from the trap

As described in Part 1, we observed a large beam spot size at the entrance of the trap electrodes, which we believe to be the reason for the low extraction efficiency. The most important thing is to reduce the diameter of the incident beam into the trap, which is at the moment 5–6 times the design value. We first need to diagnose the energy spread of the AD beam after the kicker magnet in our extraction line. Measurement of the time structure of microbunchs should give a direct information on the beam quality. It is also important to understand whether the transverse emittance blows up in the RFQD, or it is already larger than that measured in the AD ring. Therefore, in 2003, we plan to install additional beam diagnostic devices along the ASACUSA beam line. We then continue our effort to compress the antiproton cloud in the trap and to improve extraction efficiency.

3.2 Ionization measurements

There is a great interest in measurements of the single and multiple ionization cross sections for impact of 1 - 20 keV antiprotons on light atoms. Especially, the single ionization cross section for helium is attracting interest from several theoretical groups [51–53]. This is because this system is the most simple and well defined case where electron-electron correlation can be studied for dynamically evolving quantal systems. The cross section has been measured down to 13 keV antiproton energy [54], but there is a substantial discrepancy between the most recent theoretical calculations and the experimental data near the low-energy range and also discrepancies among the various theoretical calculations. As reported in the present ASACUSA progress report, the experimental apparatus is ready for these measurements and awaits the development of improved techniques for the extraction of low energy antiprotons from the ASACUSA Penning trap.

References

[1] M. Hori, J. Eades, E. Widmann, H. Yamaguchi, J. Sakaguchi, T. Ishikawa, R.S. Hayano, H.A. Torii, B. Juhász, D. Horváth, and T. Yamazaki, Phys. Rev. Lett. **87** (2001) 093401.

[2] D. Bakalov, B. Jeziorski, T. Korona, K. Szalewicz, and E. Tchoukova, Phys. Rev. Lett. **84** (2000) 2350.

[3] Y. Kino, M. Kamimura, and H. Kudo, Hyperfine Interactions **119** (1999) 201; (private communication).

[4] E. Widmann, J. Eades, T. Ishikawa, J. Sakaguchi, T. Tasaki, H. Yamaguchi, R.S. Hayano, M. Hori, H.A. Torii, B. Juhász, D. Horváth and T. Yamazaki, Phys. Rev. Lett. **89** (2002) 243402.

[5] V.I. Korobov, Phys. Rev. A **54** (1996) R1749.

[6] V.I. Korobov and D.D. Bakalov, Phys. Rev. Lett. **79**, (1997) 3379; (private communication).

[7] H. A. Torii, R.S. Hayano, M. Hori, T. Ishikawa, N. Morita, M. Kumakura, I. Sugai, T. Yamazaki, B. Ketzer, F.J. Hartmann, T. von Egidy, R. Pohl, C. Maierl, D. Horváth, J. Eades, and E. Widmann, Phys. Rev. A **59** (1999) 223.

[8] R.J. Hughes and B.I. Deutch, Phys. Rev. Lett. **69** (1992) 578.

[9] G. Gabrielse, A. Khabbaz, D.S. Hall, C. Heimann, H. Kalinowsky, and W. Jhe, Phys. Rev. Lett. **82** (1999) 3198.

[10] R. Landua and E. Klempt, Phys. Rev. Lett. **48** (1982) 1722.

[11] T. B. Day, G. A. Snow, and J. Sucher, Phys. Rev. Lett. **3** (1959) 61.

[12] G. Reifenröther, E. Klempt, and R. Landua, Phys. Lett. B **203** (1988) 9.

[13] T.S. Jensen and V.E. Markushin, (private communication).

[14] M. Hori, J. Eades, R.S. Hayano, T. Ishikawa, J. Sakaguchi, T. Tasaki, E. Widmann, H. Yamaguchi, H.A. Torii, B. Juhász, D. Horváth and T. Yamazaki, Phys. Rev. Lett. **89** (2002) 093401.

[15] E. Fermi and E. Teller, Phys. Rev **72** (1947) 399.

[16] M. Hori, H.A. Torii, R.S. Hayano, T. Ishikawa, F.E. Maas, H. Tamura, B. Ketzer, F.J. Hartmann, R. Pohl, C. Maierl, M. Hasinoff, T. von Egidy, M. Kumakura, N. Morita, I. Sugai, D. Horváth, E. Widmann, J. Eades, and T. Yamazaki, Phys. Rev. A **61** 1698 (1998); **58** (1998) 1612(E).

[17] H. Yamaguchi, T. Ishikawa, J. Sakaguchi, E. Widmann, J. Eades, R.S. Hayano, H.A. Torii, B. Juhász, D. Horváth and T. Yamazaki, Phys. Rev. A. **66** (2002) 022504.

[18] O.I. Kartavtsev, D.E. Monakhov and S.I. Fedotov, Phys. Rev. A. **61** (2000) 062507; 019901(E).

[19] V.I. Korobov and I. Shimamura, Phys. Rev. A. **56** 4587 (1997).

[20] T. Yamazaki, E. Widmann, R.S. Hayano, M. Iwasaki, S.N. Nakamura, K. Shigaki, F.J. Hartmann, H. Daniel, T. von Egidy, P. Hofmann, Y.-S. Kim, and J. Eades, Nature **361** (1993) 238.

[21] S.N. Nakamura, R.S. Hayano, M. Iwasaki, K. Shigaki, E. Widmann, T. Yamazaki, H. Daniel, T. von Egidy, F.J. Hartmann, P. Hofmann, Y.-S. Kim, and J. Eades, Phys. Rev. A **49** (1994) 4457.

[22] E. Widmann, I. Sugai, T. Yamazaki, R.S. Hayano, M. Iwasaki, S.N. Nakamura, H. Tamura, T.M. Ito, A. Kawachi, N. Nishida, W. Higemoto, Y. Ito, N. Morita, F.J. Hartmann, H. Daniel, T. von Egidy, W. Schmid, J. Hoffmann, and J. Eades, Phys. Rev. A **53** (1996) 3129.

[23] R. Pohl, F.J. Hartmann, B. Ketzer, T. von Egidy, C. Maierl, J. Eades, E. Widmann, T. Yamazaki, M. Kumakura, N. Morita, R.S. Hayano, M. Hori, T. Ishikawa, H. A. Torii, I. Sugai, and D. Horváth, Phys. Rev. A **58** (1998) 4406.

[24] T. Yamazaki, B. Ketzer, E. Widmann, J. Eades, H. Daniel, F.J. Hartmann, M. Hasinoff, R. Pohl, R. Schmidt, T. von Egidy, D. Horváth, M. Kumakura, N. Morita, I. Sugai, Y. Fujita, H.A. Torii, M. Hori, T. Ishikawa, F.E. Maas, H. Tamura, and R.S. Hayano, Chem. Phys. Lett. **265** (1997) 137.

[25] B. Ketzer, F.J. Hartmann, T. von Egidy, C. Maierl, R. Pohl, J. Eades, E. Widmann, T. Yamazaki, M. Kumakura, N. Morita, R.S. Hayano, M. Hori, T. Ishikawa, H.A. Torii, I. Sugai, and D. Horváth, J. Chem. Phys. **109** (1998) 424.

[26] B. Ketzer, T. von Egidy, F.J. Hartmann, C. Maierl, R. Pohl, J. Eades, E. Widmann, T. Yamazaki, M. Kumakura, N. Morita, R.S. Hayano, M. Hori, T. Ishikawa, H.A. Torii, I. Sugai, and D. Horváth, Eur. Phys. J. D **13** (2001) 305.

[27] B. Juhász, J. Eades, R.S. Hayano, M. Hori, D. Horváth, T. Ishikawa, J. Sakaguchi, H. A. Torii, E. Widmann, H. Yamaguchi, and T. Yamazaki, Eur. Phys. J. D **18** (2002) 261.

[28] S. Sauge and P. Valiron, Chem. Phys. **283** (2002) 433.

[29] J. B. Hasted, *Physics of atomic collisions*, 2nd edn. (Butterworth & Co., London, 1972).

[30] R.S. Hayano, F.E. Maas, H.A. Torii, N. Morita, M. Kumakura, T. Yamazaki, H. Masuda, I. Sugai, F.J. Hartmann, H. Daniel, T. von Egidy, B. Ketzer, W. Müller, W. Schmid, D. Horváth, J. Eades, and E. Widmann, Phys. Rev. Lett. **73** (1994) 1485; Errata **73** (1994) 3181.

[31] B. Ketzer, F.J. Hartmann, T. von Egidy, C. Maierl, R. Pohl, J. Eades, E. Widmann, T. Yamazaki, M. Kumakura, N. Morita, R.S. Hayano, M. Hori, T. Ishikawa, H.A. Torii, I. Sugai, and D. Horváth, Phys. Rev. Lett. **78** (1997) 1671.

[32] J. Emsley, *The Elements*, 3rd edn. (Academic Press, Oxford, 1996).

[33] P.C. Weast (editor), *Handbook of Chemistry and Physics*, 70th edn. (CRC Press, Boca Raton, 1990).

[34] H. Higaki and A. Mohri, J.J.Appl.Phys. **36** (1997) 5300.

[35] A. Mohri, H. Higaki, H. Tanaka, Y. Yamazawa, M. Aoyagi, T. Yuyama, and T. Michishita, J.J.Appl.Phys. **37** (1998) 664.

[36] K. Yoshiki Franzen, N. Kuroda, H. A. Torii, M. Hori, Z. Wang, H. Higaki, S. Yoneda, B. Juhász, D. Horváth, A. Mohri, K. Komaki and Y. Yamazaki, submitted to Review of Scientific Instruments.

[37] H.H. Andersen, A. Csete, T. Ichioka, H. Knudsen, S.P. Møller, U.I. Uggerhøj, Nucl. Instrum. Methods Phys. Res. B **194** (2002) 217.

[38] S.P Møller, A. Csete, T. Ichioka, H. Knudsen, U.I. Uggerhøj, and H.H. Andersen, Phys. Rev. Lett. **88** (2002) 193201-01.

[39] A. H. Sorensen, Nucl. Instrum. Methods Phys. Res. B **48** (1990) 10.

[40] P. Sigmund and A. Schinner, Eur. Phys. J. D **15** (2001) 165 and Nucl. Instrum. Methods. Phys. Res. B **193** (2002) 49.

[41] ICRU (International Commision for Radiation Units) Report **49**, *Stopping Powers and Ranges for Protons and Alpha Particles*, 0-913394-47-5 (1993).

[42] K. Eder et al., Phys. Rev. Lett. **79** (1997) 4112.

[43] ASACUSA collaboration, *Atomic Spectroscopy and Collisions using Slow Antiprotons* CERN-SPSC-97-19 (1997).

[44] E. Widmann, J. Eades, T. Ishikawa, J. Sakaguchi, T Tasaki, H. Yamaguchi, R.S. Hayano, M. Hori, H. A. Torii, B. Juhász, D. Horváth, and T. Yamazaki, Phys. Rev. Lett **89** (2002) 243402.

[45] D. Bakalov and V. I. Korobov, Phys. Rev. A **57** (1998) 1662.

[46] V. Korobov and D. Bakalov, J. Phys. B: At. Mol. Opt. Phys. **34** (2001) L519.

[47] Y. Kino, N. Yamanaka, M. Kamimura, and H. Kudo, in *Proceedings of the 3rd European Conference on Atomic Physics at Accelerators (APAC2001)*, Aarhus, Denmark, 2001, Hyperfine Interactions, in press.

[48] A. Kreissl *et al.*, Z. Phys. C **37** (1988) 557.

[49] G. Ya. Korenman (private communication).

[50] D. Bakalov (private communication).

[51] A. Igarashi, *Ionization cross sections of helium and hydrogenic ions by antiproton impact*, submitted to the International Conference on Low Energy Antiproton Physics, Yokohama, Japan, March 2003.

[52] M. Keim, A. Achenbach, T. Kirchner, H.J. Lüdde and R.M. Dreizler, *Single Ionization in Collisions of Antiprotons with Helium*, submitted to the International Conference on Low Energy Antiproton Physics, Yokohama, Japan, March 2003

[53] S. Morita, N Matsuda and N. Toshima, *Double- to single ionization ratio of helium atoms by proton and antiproton impact*, submitted to the International Conference on Low Energy Antiproton Physics, Yokohama, Japan, March 2003

[54] ASACUSA collaboration, *ASACUSA Status report*, CERN/SPSC 2002 - 002 SPSC M674